The Interpolated Local Model Fitting Method for Accurate and Fast Single-shot Surface Profiling

Tatsuya Yokota
Tokyo Institute of Technology
2-12-1-W8-74 O-okayama, Meguro-ku, Tokyo, 152-8552, Japan.
yokota@yy.ide.titech.ac.jp

Masashi Sugiyama
Tokyo Institute of Technology
2-12-1 O-okayama, Meguro-ku, Tokyo 152-8552, Japan.
sugi@cs.titech.ac.jp   http://sugiyama-www.cs.titech.ac.jp/~sugi

Hidemitsu Ogawa
Toray Engineering Co., Ltd.
1-1-45 Oe, Otsu, Shiga, 520-2141, Japan.
hidemitsu-ogawa@kuramae.ne.jp

Katsuichi Kitagawa
Toray Engineering Co., Ltd.
1-1-45 Oe, Otsu, Shiga, 520-2141, Japan.
Katsuichi_Kitagawa@toray-eng.co.jp

Kazuyoshi Suzuki
Toray Engineering Co., Ltd.
1-1-45 Oe, Otsu, Shiga, 520-2141, Japan.
Kazuyoshi_Suzuki@toray-eng.co.jp

Abstract

The local model fitting (LMF) method is a useful single-shot surface profiling algorithm based on spatial carrier frequency fringe patterns. The measurement principle of the LMF method relies on the assumption that the target surface is locally flat. In this paper, we first analyze the measurement error of the LMF method caused by violation of the locally flat assumption. More specifically, we theoretically prove that the measurement error is zero at fringe intensity extrema in an interference pattern even when the locally flat assumption is violated. Based on this theoretical finding, we propose a new surface profiling method called the interpolated LMF (iLMF) algorithm which is more accurate and computationally efficient than the original LMF method. The practical usefulness of the iLMF method is shown through experiments.

1   Introduction

We address the problem of estimating the surface profile of a target object using an optical interferometer with a *tilted* reference mirror. Such a device allows one to recover the surface profile solely from a single image. Several single-shot methods based on spatial carrier frequency fringe patterns have been developed so far, for example, the *Fourier transform method* [1], the *spatial phase synchronization method* [2], the *spatial phase-shift method* [3, 4], and the *local model fitting (LMF) method* [5].

One of the advantages of single-shot methods over multiple-shot methods such as the *phase shift method* [6, 7] is their inherent immunity to vibration. Furthermore, the measurement system of single-shot methods is simpler since mechanical devices such as piezo actuators are not needed. Among various single-shot methods developed so far, the LMF method [5] is shown to be more useful than other methods since one can measure the surface profile of an object with sharp steps (which is an advantage over the Fourier transform method [1] and the spatial phase synchronization method [2]) and the tilting angle could be arbitrary (which is an advantage over the spatial phase-shift method [3, 4]).

The measurement principle of the LMF method relies on the assumption that the target surface is locally flat. Based on this locally flat assumption, unknown parameters in the fringe model such as the bias and the amplitude are reliably estimated from the target and surrounding pixels in the observed interference pattern. However, when the locally flat assumption is violated, the accuracy of the LMF method can be degraded. For example, when the surface profile illustrated in Figure 3(a) is measured by the LMF method, the estimated profile is inaccurate as illustrated in Figure 5(a).

The goal of this paper is to overcome this drawback of the LMF method and develop a new surface profiling algorithm. To this end, we first analyze the measurement error of the LMF method caused by violation of the locally flat assumption. More specifically, we theoretically prove that the measurement error becomes zero at fringe intensity extrema (i.e., minima and maxima; see Figure 4(a)) of an interference pattern.

Based on the theoretical finding, we propose an improved algorithm of the LMF method which we refer to as the *interpolated LMF* (iLMF). The basic idea of the iLMF method is to only use pixels in the interference pattern around fringe intensity extrema for estimating the surface profile; the surface profile at other pixels are interpolated from the estimates at the extremum pixels (see Figure 5(b)). This highly contributes to reducing the estimation error and, at the same time, improving the computational efficiency since only a small portion of pixels in the interference pattern needs to be processed. We demonstrate the usefulness of the iLMF algorithm through measurement experiments.

The rest of this paper is organized as follows. In Section 2, the original LMF method is briefly reviewed. In Section 3, a theoretical error analysis of the LMF method under violation of the locally flat assumption is carried out and the iLMF algorithm is introduced. Experimental results are reported in Section 4, and concluding remarks are given in Section 5.

2   The Local Model Fitting Algorithm

In this section, we review a single-shot surface profiling algorithm called the LMF method [5].

   We tilt the reference mirror in an arbitrary angle. Then the model of an interference pattern is given as follows [1, 2, 3, 4]:

$$g(x,y) := a(x,y) + b(x,y)\cos\Big(\phi(x,y) + 2\pi f_{\mathrm{x}}x + 2\pi f_{\mathrm{y}}y\Big),$$

where $a(x,y)$ and $b(x,y)$ are the bias and the amplitude, $\phi(x,y)$ contains the information on the surface profile which we would like to extract, and f_{x} and f_{y} are the spatial carrier frequencies along the x-axis and y-axis, respectively. We can easily show that $g(x,y)$ can be equivalently expressed as

$$g(x,y) = a(x,y) + \xi_{\mathrm{c}}(x,y)\varphi_{\mathrm{c}}(x,y) + \xi_{\mathrm{s}}(x,y)\varphi_{\mathrm{s}}(x,y),$$

where

$$\xi_{\mathrm{c}}(x,y) := b(x,y)\cos\phi(x,y), \qquad \varphi_{\mathrm{c}}(x,y) := \cos(2\pi f_{\mathrm{x}}x + 2\pi f_{\mathrm{y}}y),$$
$$\xi_{\mathrm{s}}(x,y) := b(x,y)\sin\phi(x,y), \qquad \varphi_{\mathrm{s}}(x,y) := -\sin(2\pi f_{\mathrm{x}}x + 2\pi f_{\mathrm{y}}y).$$

   Suppose we have samples $\{g(x_i,y_i)\}_{i=1}^{n}$ in the vicinity of a point of interest (x_0,y_0). Our goal is to estimate $\phi(x_0,y_0)$ from $\{g(x_i,y_i)\}_{i=1}^{n}$. Here we make the following assumption: $a(x,y)$, $b(x,y)$, and $\phi(x,y)$ are constant in the vicinity of (x_0,y_0), i.e., our *local* model is given by

$$g(x,y) = a + \xi_{\mathrm{c}}\varphi_{\mathrm{c}}(x,y) + \xi_{\mathrm{s}}\varphi_{\mathrm{s}}(x,y), \tag{1}$$

where

$$\xi_{\mathrm{c}} := b\cos\phi \quad\text{and}\quad \xi_{\mathrm{s}} := b\sin\phi. \tag{2}$$

   Suppose we have reasonable estimates of the spatial carrier frequencies f_{x} and f_{y}, denoted by $\widehat{f}_{\mathrm{x}}$ and $\widehat{f}_{\mathrm{y}}$, respectively; $\widehat{f}_{\mathrm{x}}$ and $\widehat{f}_{\mathrm{y}}$ may be obtained from the fringe image of a flat area. Note that the spatial carrier frequencies f_{x} and f_{y} are global quantities which do not depend on the target object and are determined by the (relative) tilting angle of the reference mirror.

   Then the unknown parameters in the simplified model (1) are only a, ξ_{c}, and ξ_{s}—they are determined by solving the following least-squares problem:

$$(\widehat{a}, \widehat{\xi}_{\mathrm{c}}, \widehat{\xi}_{\mathrm{s}}) := \operatorname*{argmin}_{(a,\xi_{\mathrm{c}},\xi_{\mathrm{s}})} \sum_{i=1}^{n} \Big(g(x_i,y_i) - a - \xi_{\mathrm{c}}\varphi_{\mathrm{c}}(x_i,y_i) - \xi_{\mathrm{s}}\varphi_{\mathrm{s}}(x_i,y_i)\Big)^2.$$

Since the above model is linear with respect to the parameters a, ξ_{c}, and ξ_{s}, the least-squares solutions $\widehat{a}$, $\widehat{\xi}_{\mathrm{c}}$, and $\widehat{\xi}_{\mathrm{s}}$ can be analytically obtained as follows [8]:

$$\begin{pmatrix}\widehat{a}\\ \widehat{\xi}_{\mathrm{c}}\\ \widehat{\xi}_{\mathrm{s}}\end{pmatrix} = (\mathbf{A}^{\top}\mathbf{A})^{-1}\mathbf{A}^{\top}\begin{pmatrix}g(x_1,y_1)\\ \vdots\\ g(x_n,y_n)\end{pmatrix},$$

where

$$\mathbf{A} := \begin{pmatrix} 1 & \varphi_{\mathrm{c}}(x_1, y_1) & \varphi_{\mathrm{s}}(x_1, y_1) \\ \vdots & \vdots & \vdots \\ 1 & \varphi_{\mathrm{c}}(x_n, y_n) & \varphi_{\mathrm{s}}(x_n, y_n) \end{pmatrix}.$$

Given $\widehat{\xi}_{\mathrm{c}}$ and $\widehat{\xi}_{\mathrm{s}}$, we can obtain an estimate $\widehat{\phi}$ of the surface profile at (x_0, y_0) by

$$\widehat{\phi} := \arctan\left(\widehat{\xi}_{\mathrm{s}}/\widehat{\xi}_{\mathrm{c}}\right) + 2m\pi,$$

where m is an unknown integer. Note that we can determine the value of arctangent upto a 2π range by using the signs of $\cos\phi$ and $\sin\phi$. Since b is always positive, the signs of $\cos\phi$ and $\sin\phi$ could be estimated by the signs of $\widehat{\xi}_{\mathrm{c}}$ and $\widehat{\xi}_{\mathrm{s}}$, respectively (cf. Eq.(2)). m may be determined by a phase-unwrapping algorithm [9, 10].

3 Improving Measurement Accuracy and Computational Efficiency of the LMF Method

The key idea of the LMF method is that $a(x, y)$, $b(x, y)$, and $\phi(x, y)$ are assumed to be constant in the vicinity of (x_0, y_0). This enables us to estimate the unknown parameters in the model at (x_0, y_0) from the observed data around (x_0, y_0). However, when the target surface is curved, the locally flat assumption (i.e., $\phi(x, y)$ is constant) may not be exactly fulfilled and therefore some measurement error is incurred. In this section, we first analyze the measurement error incurred by violation of the locally flat assumption theoretically. Then, based on this theoretical result, we develop a more accurate and computationally efficient algorithm called the iLMF method.

3.1 Theoretical Error Analysis of the LMF Method

For making the analysis simple, let us assume that the vicinity data are taken only along the x-axis in an equidistant manner; more specifically, the vicinity data are taken as $\{g(x_i, y_0)\}_{i=-n}^{n}$, where for $\Delta x \ (> 0)$,

$$x_i = x_0 + i\Delta x.$$

For brevity, we omit y_0 below; then the fringe intensity at x_0 is expressed as

$$g(x_0) = a + b\cos(\theta),$$

where

$$\theta := \phi(x_0) + 2\pi f x_0.$$

We assume that the bias $a(x)$ and the amplitude $b(x)$ are locally constant around x_0, and analyze the measurement error when $\phi(x, y)$ is not locally constant around x_0.

Let us define the measurement error at x_0 by

$$\varepsilon := \widehat{\phi} - \phi. \tag{3}$$

Then if terms with $\mathcal{O}(\Delta x^5)$ are ignored, $\tan \varepsilon$ can be expressed as

$$\tan \varepsilon = \frac{S(1 - \cos 2\theta) - R \sin 2\theta}{1 + R(1 + \cos 2\theta) - S \sin 2\theta}, \tag{4}$$

where R and S depend on the unknown surface profile $\{\phi(x_i)\}_{i=-n}^{n}$. The detailed definitions of R and S as well as the derivation of Eq.(4) are summarized in Appendix A.

3.2 The iLMF Algorithm

Equation (4) implies that the error ε becomes zero if

$$\theta = m\pi \tag{5}$$

with m being an integer. An important observation is that Eq.(5) can be fulfilled *without* knowing the true surface profile $\{\phi(x_i)\}_{i=-n}^{n}$. Indeed, setting x_0 to fringe intensity *extrema* (i.e., minima and maxima; see Figure 4) in the interference pattern satisfies Eq.(5).

So our finding above can be summarize as follows:

> *At any fringe intensity minimum and maximum of the interference pattern, the measurement error is always zero even when the locally flat assumption is violated.*

Based on this result, we propose to compute the LMF solutions only at fringe intensity extrema of the interference pattern; the surface estimates at other points are interpolated, e.g., linearly or by some spline methods [11]. We call this algorithm the *interpolated LMF* (iLMF) method. This will improve the measurement accuracy of the LMF method. The computational efficiency might be affected by the algorithm for the localization of the extrema.

The period of fringe intensity extrema depends on the spatial carrier frequencies; if the reference mirror is tilted strongly, then we have many fringe intensity extrema and thus measurement results will be more accurate.

3.3 Geometric Interpretation

In the rest of this section, we give a geometric interpretation of the above theoretical result. Those who are interested in the experimental performance of the iLMF method may skip the rest of this section.

In the LMF method, the unknown quantities ξ_c and ξ_s at x_0 in the model of interference patterns are estimated by least-squares fitting based on the locally flat assumption. Let us define the error caused by the estimates $\widehat{\xi}_c$ and $\widehat{\xi}_s$ as

$$\Delta \xi_c := \widehat{\xi}_c - \xi_c \quad \text{and} \quad \Delta \xi_s := \widehat{\xi}_s - \xi_s.$$

Below, we use vector notation:

$$\Delta\boldsymbol{\xi} := \begin{pmatrix} \Delta\xi_c \\ \Delta\xi_s \end{pmatrix}, \quad \widehat{\boldsymbol{\xi}} := \begin{pmatrix} \widehat{\xi}_c \\ \widehat{\xi}_s \end{pmatrix}, \quad \text{and} \quad \boldsymbol{\xi} := \begin{pmatrix} \xi_c \\ \xi_s \end{pmatrix}.$$

Then, as detailed in Appendix B, we have

$$\Delta\boldsymbol{\xi} \propto \boldsymbol{\xi}_\beta + \boldsymbol{\xi}_{-\beta-2\theta}, \tag{6}$$

where $\boldsymbol{\xi}_\beta$ denotes a rotated vector of $\boldsymbol{\xi}$ by angle β and

$$\beta := \arctan(S/R).$$

Note that β is not accessible since R and S are unknown.

Equation (6) shows that the vector $\Delta\boldsymbol{\xi}$ is proportional to the sum of $\boldsymbol{\xi}$ rotated by $-\beta - 2\theta$ and $\boldsymbol{\xi}$ rotated by β (see Figure 1). Since the measurement error ε is the angle between $\widehat{\boldsymbol{\xi}}$ and $\boldsymbol{\xi}$ (see Eq.(3) and Figure 1), it vanishes if and only if $\widehat{\boldsymbol{\xi}}$ and $\boldsymbol{\xi}$ are parallel or $\|\Delta\boldsymbol{\xi}\| = 0$ (i.e., the parameter estimation error is zero). As illustrated in Figure 2, this is achieved either when

$$\theta = m\pi \quad (\widehat{\boldsymbol{\xi}} \text{ and } \boldsymbol{\xi} \text{ point to the same direction}),$$

or

$$\theta = \frac{(2m+1)\pi}{2} - \beta \quad (\|\Delta\boldsymbol{\xi}\| \text{ vanishes}),$$

where m is an arbitrary integer. The first condition can be fulfilled without the knowledge of β, while the second condition may not be useful in practice since β is unknown.

4   Experiments

In this section, we report experimental results of the iLMF algorithm. For simplicity, we use naive linear interpolation for the iLMF method.

4.1   Computer Simulations

First, we illustrate the behavior of the iLMF algorithm through one-dimensional computer simulations. Let us consider two target surfaces: a quadratic function and a sharp bump illustrated in Figure 3(a) and Figure 3(b), respectively. Note that the locally flat assumption is not exactly satisfied everywhere in the quadratic function and it is satisfied in the bump except for the regions around the sharp edges. The interference patterns of these surfaces are depicted in Figure 4(a) and Figure 4(b), respectively, where the circles ('○') denote the fringe intensity extrema of the interference patterns.

The estimated surfaces of the quadratic function obtained by the LMF and iLMF algorithms with vicinity size $n = 10$ (i.e., 21 points) are depicted in Figure 5(a) and
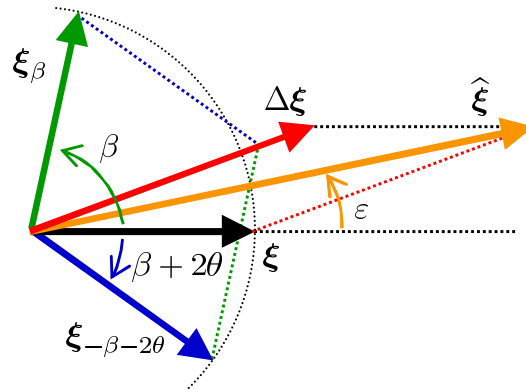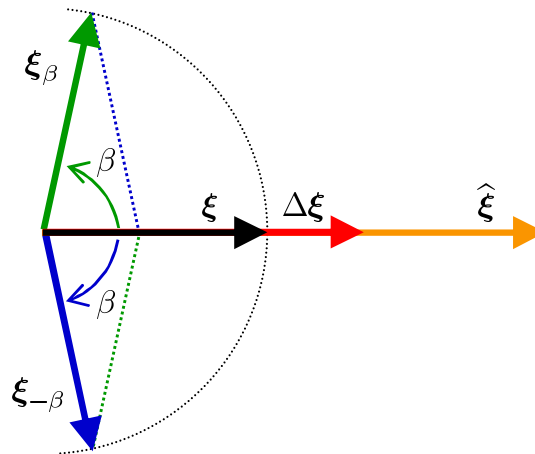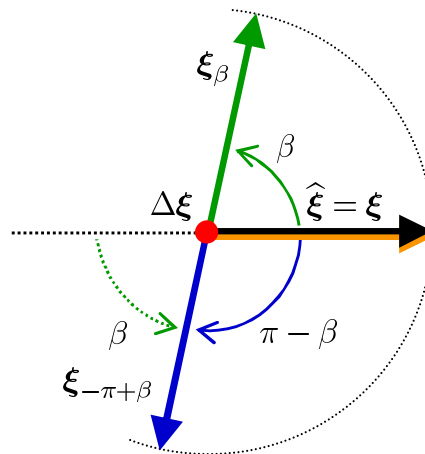
Figure 1: Geometric interpretation. $\boldsymbol{\xi}_\beta$ denotes a rotated vector of $\boldsymbol{\xi}$ by angle β. The measurement error ε is the angle between $\widehat{\boldsymbol{\xi}}$ and $\boldsymbol{\xi}$.

(a) $\widehat{\boldsymbol{\xi}}$ and $\boldsymbol{\xi}$ point to the same direction.

(b) $\|\Delta\boldsymbol{\xi}\|$ vanishes.

Figure 2: Geometric interpretation when the measurement error ε is zero.
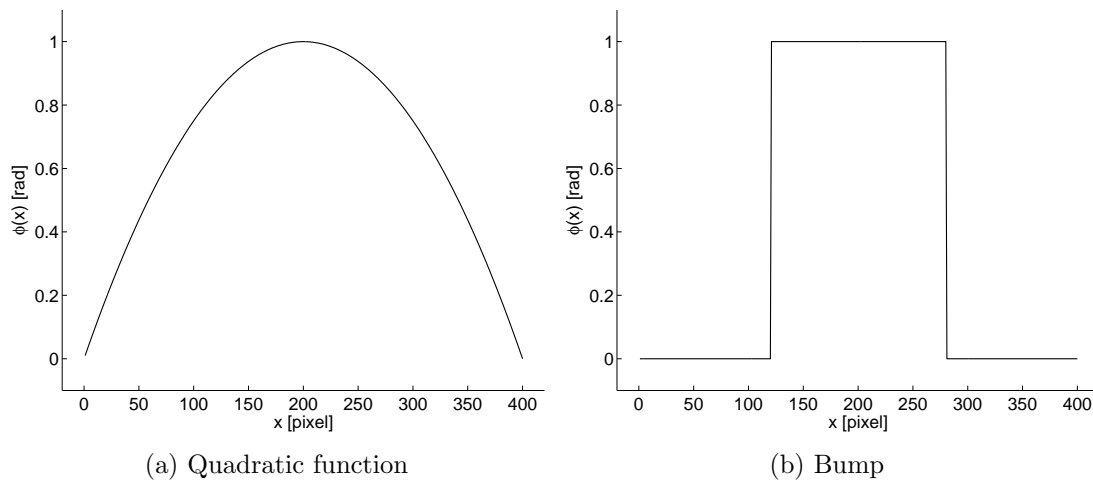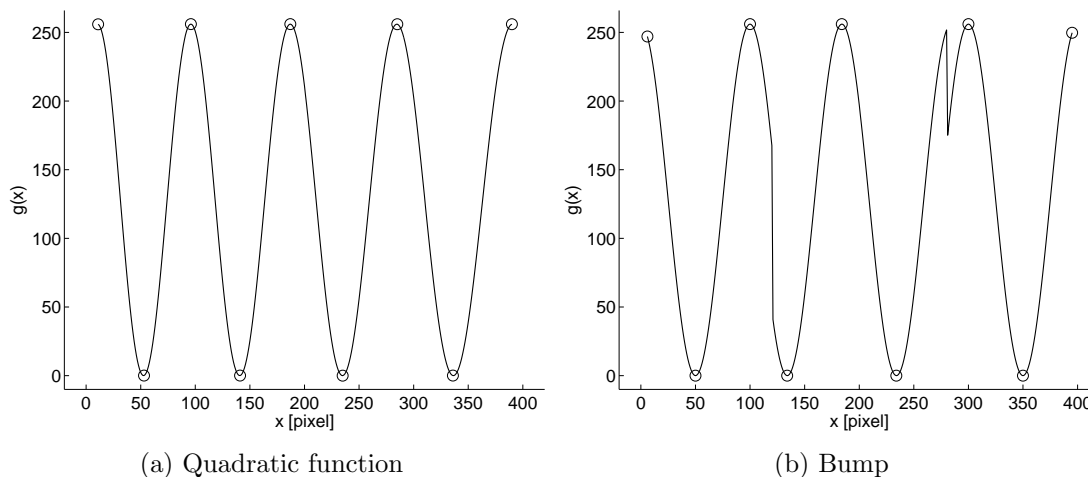
(a) Quadratic function

(b) Bump

Figure 3: True surface profile $\phi(x)$ in artificial one-dimensional experiments.

(a) Quadratic function

(b) Bump

Figure 4: Observed interference pattern $g(x)$ in artificial one-dimensional experiments.

Figure 5(b), respectively. Figure 5(a) shows that the recovered surface is highly fluctuated due to violation of the locally flat assumption. Figure 5(b) shows that estimation results at the extremum points (9 points indicated by '∘') are very accurate and the interpolated surface profile is less fluctuated than the surface profile estimated by the original LMF method.

Figure 6(a) depicts the 'raw' estimation result of the bump by the LMF algorithm with vicinity size $n = 5$ (i.e., 11 points). The recovered surface is very accurate in the flat areas, while it is noisy at the edges—this is due to violation of the locally flat assumption. Figure 6(b) depicts the post-processed result of Figure 6(a) by the *median filter* with width 20 (i.e., 41 points), showing that the impulse-like noise at the edges can be successfully removed. However, the application of median filters is generally computationally expensive. Figure 6(c) depicts the estimation result by the iLMF algorithm.
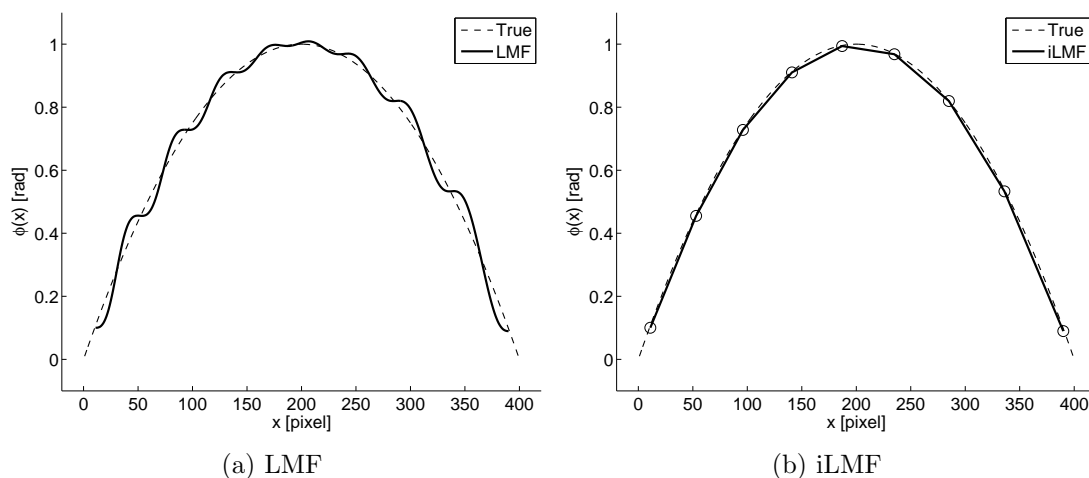
(a) LMF

(b) iLMF

Figure 5: Recovered surface of the quadratic function.

Although the iLMF algorithm is shown not to suffer from impulse noise, interpolation causes degradation in spacial resolution. The spacial resolution can easily be enhanced by increasing the spacial carrier frequency, which can be achieved by tilting the reference mirror strongly. Figure 6(d) depicts the result of the iLMF algorithm with a high spacial carrier frequency. This shows that the quality of the recovered surface is highly improved *without* the use of median filters which requires high computation resources.

4.2   Actual Experiments

We installed the iLMF algorithm in the optical surface profiler *SP-500* by Toray Engineering Co., Ltd.[1]. Each pixel takes an integer value from 0 to 255 (i.e., 8-bit intensity). We measured the surface of a magnetic head and a bump—we have prior knowledge that the magnetic head possesses a smooth arch-like profile and the bump is sharp with the flat top. Figure 7(a) and Figure 7(b) depict fringe images $g(x, y)$ of the magnetic head and the bump obtained by SP-500; the size of the images is 200 by 50 and 70 by 35, respectively.

Figure 8 and Figure 9 depict the surfaces of the magnetic head recovered by the LMF method and the iLMF method, respectively; we set the vicinity window size to 21 by 21. These figures show that the iLMF method gives a smoother surface with less fluctuation than the original LMF method. Thus the iLMF method can overcome the weakness of the LMF method against violation of the locally flat assumption. The computation time of the LMF algorithm for this experiment is 0.78[sec] by a modern laptop computer, while the computation time of the iLMF algorithm is 0.16[sec]. Thus the iLMF algorithm is approximately five times faster than the LMF algorithm. This speed-up is brought by the fact that the number of points to be processed is much smaller in the iLMF algorithm.

Figure 10 and Figure 11 depict the surfaces of the bump recovered by the LMF method,

---

[1]See 'http://www.toray-eng.co.jp/semicon/inspection/lineup/sp-500.html' for detail.

(a) LMF

(b) Median-filtered LMF

(c) iLMF

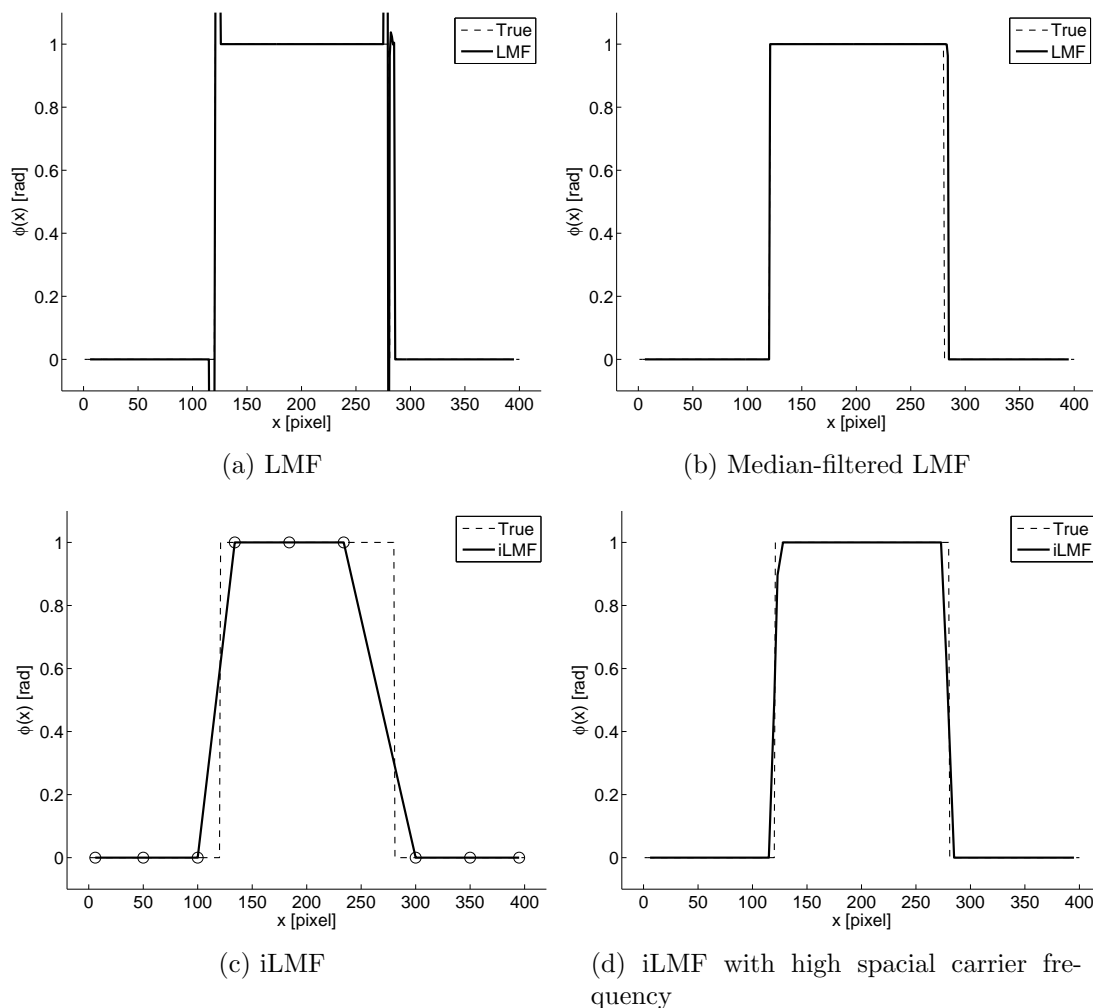(d) iLMF with high spacial carrier frequency

Figure 6: Recovered surface of the bump.

the LMF method followed by the application of a median filter, and the iLMF method, respectively; we set the window size of the vicinity to 5 by 5 and the window size of the median filter to 7 by 7. The measurement result obtained by the LMF method is depicted in Figure 10(a), exhibiting two sources of estimation error: an impulse-like error at the sharp edge around $x = 60$ and a small error at the gentle slope around $x = 25$ (see also Figure 11(a)). The impulse-like error at the edge can be successfully removed by the application of the median filter, as shown in Figure 10(b) and Figure 11(b). However, the error at the slope still remains even after the application of the median filter. On the other hand, the proposed iLMF method can successfully eliminate both estimation errors and gives a sharper profile, as shown in Figure 10(c) and Figure 11(c).

The computation time of the LMF, median-filtered LMF, and iLMF methods are 0.14[sec], 0.22[sec], and 0.09[sec], respectively. Thus the iLMF algorithm is still computationally more efficient than the LMF algorithm. This speed-up is brought by the facts
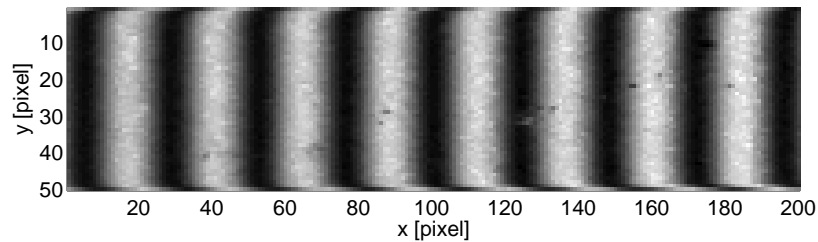
(a) Fringe image of the magnetic head
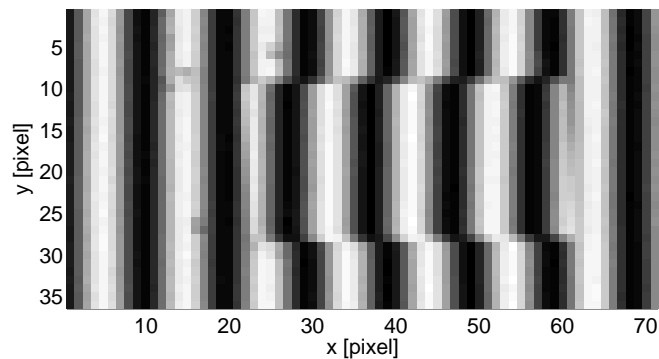
(b) Fringe image of the bump

Figure 7: Interferometer and fringe images.

that the number of points to be processed is much smaller in the iLMF algorithm and the post-processing by the median filter is not needed.

5 Conclusions

Single-shot surface profiling based on spatial carrier frequency fringe patterns is useful in real-world situations due to its inherent immunity to vibration; moreover, the measurement system of single-shot surface profilers tends to be simpler than that of the multiple-shot profilers since mechanical devices such as piezo actuators are not needed. In this paper, we first analyzed the measurement error of a single-shot surface profiling algorithm called the *local model fitting* (LMF) algorithm [5]. Our theoretical result showed that although the error depends on the unknown target surface, it can be minimized with respect to the measurement location *without* knowing the true surface; we also provided a geometric interpretation of the mechanism why this is possible.

This theoretical result showed that at fringe intensity extrema (minima and maxima) of an interference pattern, the measurement error is always zero irrespective of the true surface profile. Based on this finding, we proposed a new single-shot surface profiling algorithm called the *interpolated LMF* (iLMF) method, which only uses pixels in the interference pattern around fringe intensity extrema for estimating the surface profile; the surface profile at other pixels are interpolated from the estimates at the extremum pixels.

Through experiments, we demonstrated that the iLMF method is more accurate than
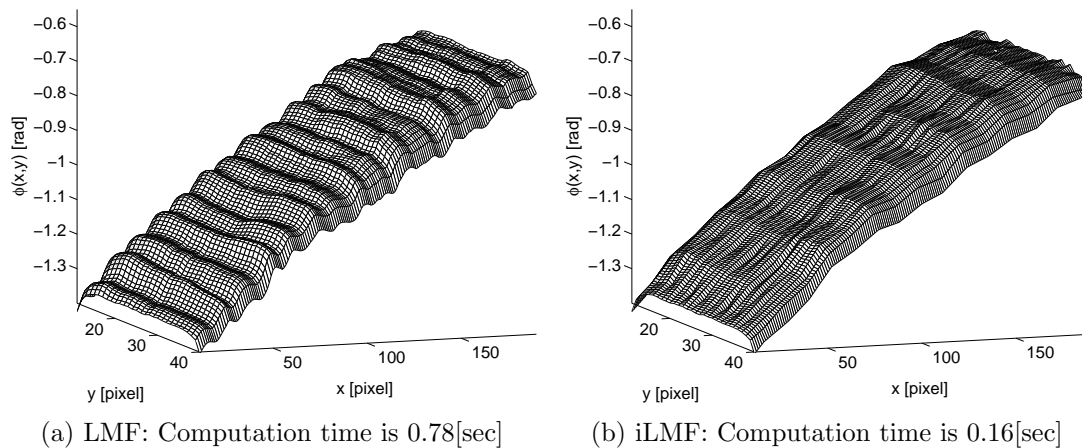
(a) LMF: Computation time is 0.78[sec] (b) iLMF: Computation time is 0.16[sec]

Figure 8: Measurement results of the actual magnetic head in 3-dimensional plots.
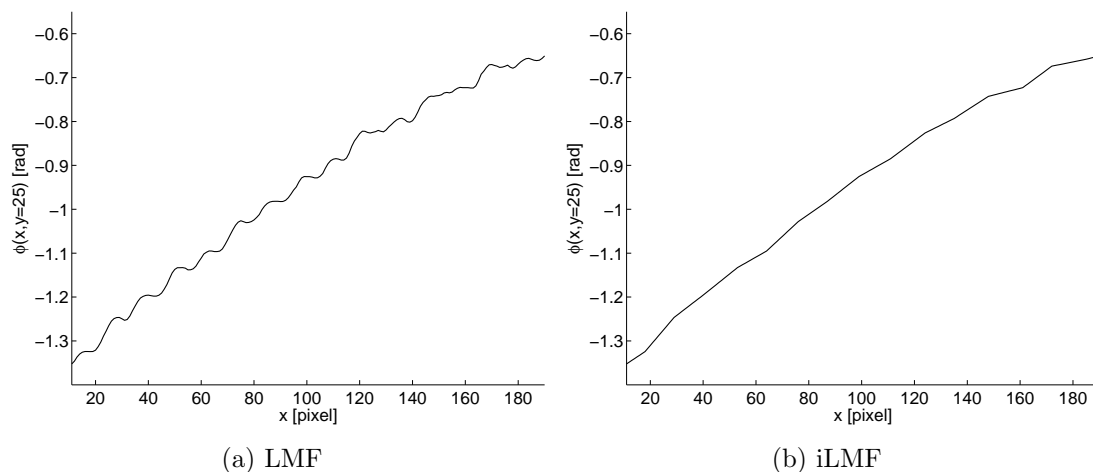

(a) LMF (b) iLMF

Figure 9: Measurement results of the actual magnetic head in 2-dimensional plots.

the original LMF method; furthermore, since only a small portion of pixels in the interference pattern needs to be processed and post-processing by median filters are not required in the iLMF method, it is computationally more efficient than the LMF method.

In our current implementation of the iLMF algorithm, extrema points are found by naively searching for locally maximal pixels. Although this naive implementation performed sufficiently well in the experiments reported in Section 4, a more sophisticated algorithm for localizing the extrema points could potentially improve the accuracy of the iLMF method, e.g., in highly noisy environment. Thus developing robust and computationally efficient algorithms for localizing the extrema points would be a promising direction for further investigation.

We have used a locally constant model (the zeroth order polynomial) in the proposed iLMF method. A natural direction for extension would be to use richer models such as

(a) LMF: Computation time is 0.14[sec]

(b) Median-filtered LMF: Computation time is 0.22[sec]

(c) iLMF: Computation time 0.09[sec]
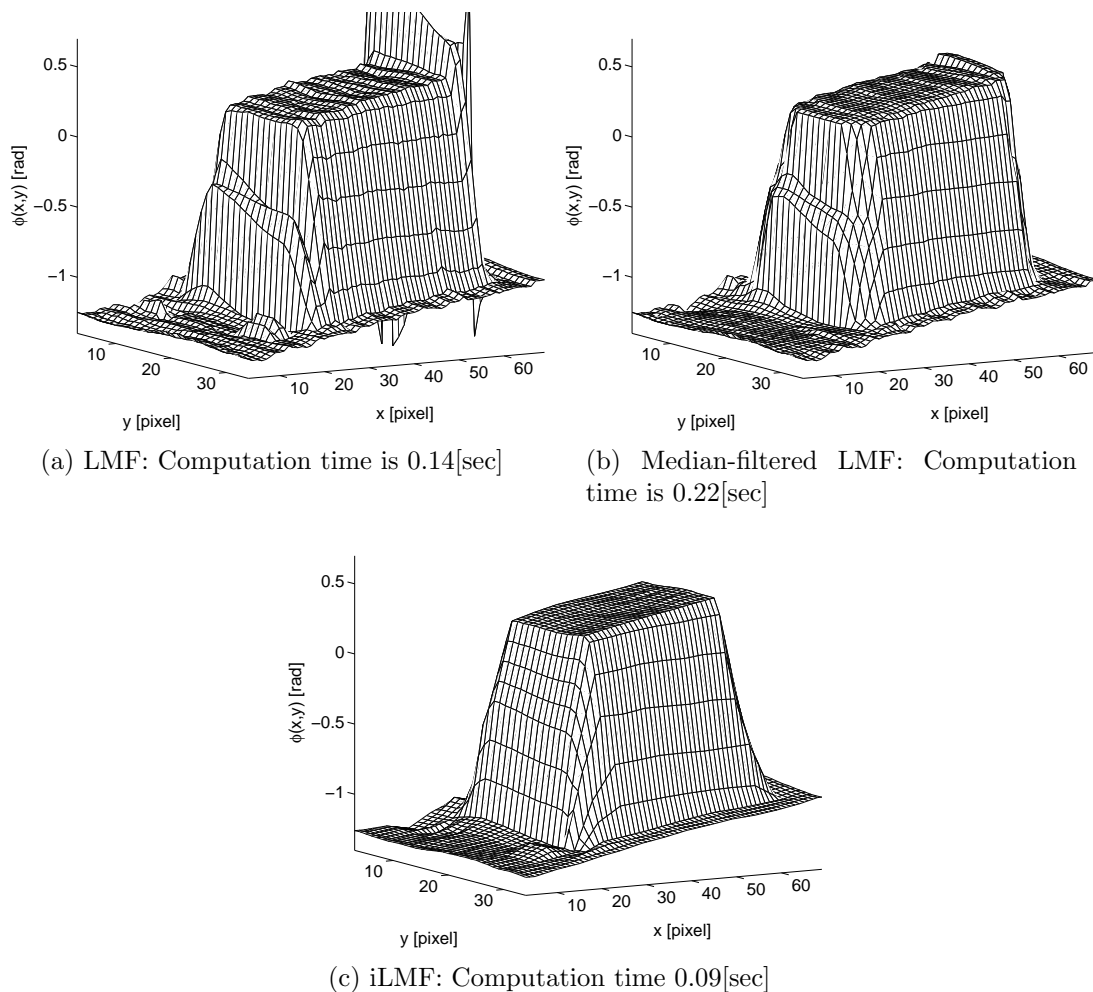
Figure 10: Measurement results of the actual bump in 3-dimensional plots.

a linear model (the first order polynomial) or even non-linear (higher order polynomials) models. In the ordinary phase-shift method (i.e., multiple shots), the use of a locally linear model has already been addressed [12]. On the other hand, in the single-shot method with a tilted reference mirror, this extension seems to be less straightforward since the locally linear term cannot be separated from the spacial carrier frequency terms (which are also linear). Our future work includes further investigation of this modeling issue.

Acknowledgements

(a) LMF

(b) Median-filtered LMF

(c) iLMF
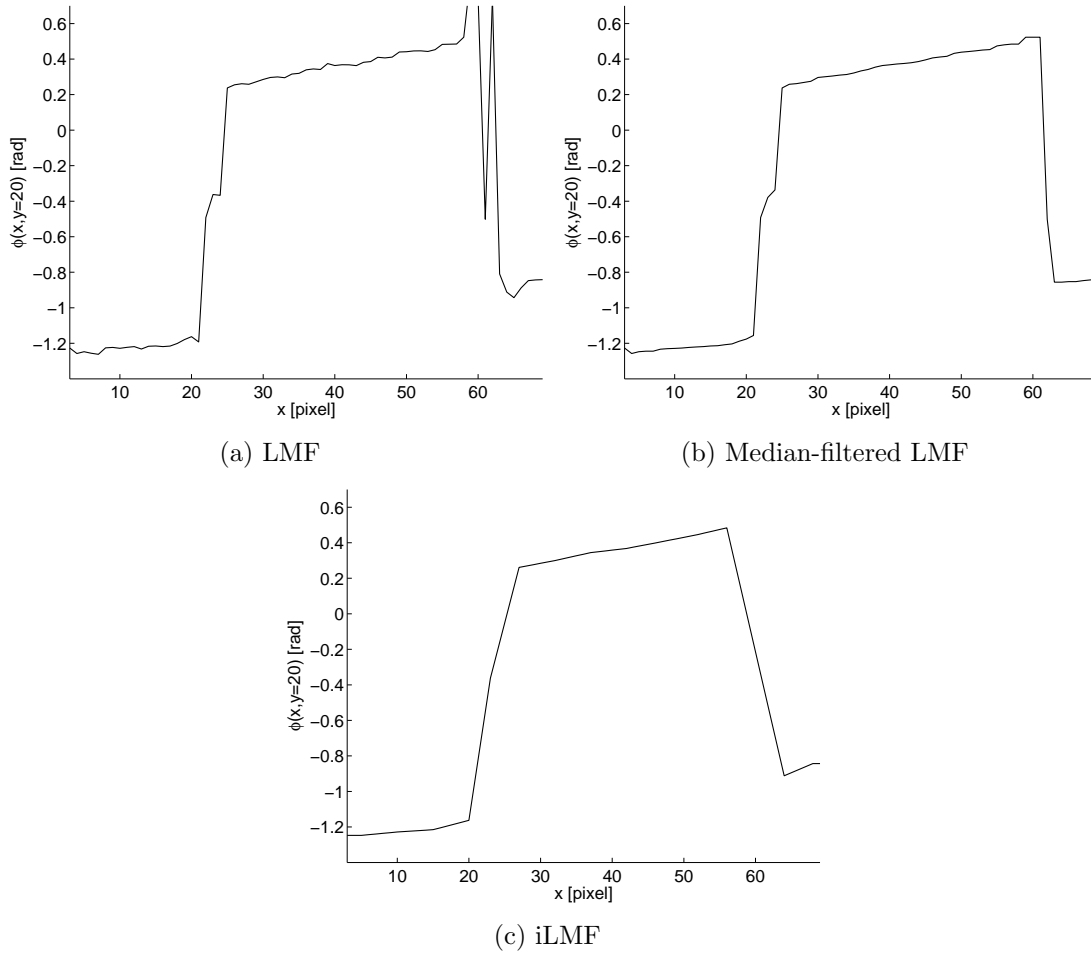
Figure 11: Measurement results of the actual bump in 2-dimensional plots.

A   Sketch of Proof of Eq.(4)

In this appendix, we give a sketch of proof of Eq.(4).

First, we define notations used in the proof. In the current setup, the observed samples $\{g(x_i)\}_{i=-n}^{n}$ are expressed as

$$g(x_i) = a(x_0) + b(x_i) \cos \left(\phi(x_i) + 2\pi f x_i \right)$$
$$= a(x_0) + \xi_c(x_i) \varphi_c(x_i) + \xi_s(x_i) \varphi_s(x_i).$$

Then the LMF estimate $\widehat{\phi}$ of the surface profile is given as

$$\widehat{\phi} = \arctan(\widehat{\xi_s}/\widehat{\xi_c}) + 2m\pi,$$

where

$$\begin{pmatrix} \widehat{a} \\ \widehat{\xi}_{\mathrm{c}} \\ \widehat{\xi}_{\mathrm{s}} \end{pmatrix} = (\mathbf{A}^{\top}\mathbf{A})^{-1}\mathbf{A}^{\top} \begin{pmatrix} g(x_{-n}) \\ \vdots \\ g(x_n) \end{pmatrix} \quad \text{and} \quad \mathbf{A} = \begin{pmatrix} 1 & \varphi_{\mathrm{c}}(x_{-n}) & \varphi_{\mathrm{s}}(x_{-n}) \\ \vdots & \vdots & \vdots \\ 1 & \varphi_{\mathrm{c}}(x_n) & \varphi_{\mathrm{s}}(x_n) \end{pmatrix}.$$

Let us consider 'ideal' samples $\{g_0(x_i)\}_{i=-n}^{n}$, where

$$g_0(x_i) := a(x_0) + \xi_{\mathrm{c}}(x_0)\varphi_{\mathrm{c}}(x_i) + \xi_{\mathrm{s}}(x_0)\varphi_{\mathrm{s}}(x_i).$$

Then the true surface profile ϕ can be expressed as

$$\phi = \arctan(\xi_{\mathrm{s}}(x_0)/\xi_{\mathrm{c}}(x_0)) + 2m\pi,$$

where

$$\begin{pmatrix} a(x_0) \\ \xi_{\mathrm{c}}(x_0) \\ \xi_{\mathrm{s}}(x_0) \end{pmatrix} = (\mathbf{A}^{\top}\mathbf{A})^{-1}\mathbf{A}^{\top} \begin{pmatrix} g_0(x_{-n}) \\ \vdots \\ g_0(x_n) \end{pmatrix}.$$

Let $\{\Delta g(x_i)\}_{i=-n}^{n}$ be the 'difference' samples:

$$\begin{aligned} \Delta g(x_i) &:= g(x_i) - g_0(x_i) \\ &= \Big(\xi_{\mathrm{c}}(x_i) - \xi_{\mathrm{c}}(x_0)\Big)\varphi_{\mathrm{c}}(x_i) + \Big(\xi_{\mathrm{s}}(x_i) - \xi_{\mathrm{s}}(x_0)\Big)\varphi_{\mathrm{s}}(x_i). \end{aligned}$$

Let $\Delta\xi_{\mathrm{c}}(x_0)$ and $\Delta\xi_{\mathrm{s}}(x_0)$ be the difference of parameters:

$$\begin{aligned} \begin{pmatrix} \Delta a(x_0) \\ \Delta\xi_{\mathrm{c}}(x_0) \\ \Delta\xi_{\mathrm{s}}(x_0) \end{pmatrix} &:= \begin{pmatrix} \widehat{a} \\ \widehat{\xi}_{\mathrm{c}} \\ \widehat{\xi}_{\mathrm{s}} \end{pmatrix} - \begin{pmatrix} a(x_0) \\ \xi_{\mathrm{c}}(x_0) \\ \xi_{\mathrm{s}}(x_0) \end{pmatrix} \\ &= (\mathbf{A}^{\top}\mathbf{A})^{-1}\mathbf{A}^{\top} \begin{pmatrix} \Delta g(x_{-n}) \\ \vdots \\ \Delta g(x_n) \end{pmatrix}. \end{aligned}$$

Let $\Delta\phi(x_i)$ be the amount of violation of the locally flat assumption:

$$\Delta\phi(x_i) := \phi(x_i) - \phi(x_0).$$

Below, we analyze the tangent of the measurement error

$$\varepsilon := \widehat{\phi} - \phi.$$

To this end, we use the following lemmas (we omit the proofs since they are rather straightforward but lengthy).

Lemma A.1 *It holds that*
$$\tan\varepsilon = \frac{\xi_{\mathrm{c}}(x_0)\Delta\xi_{\mathrm{s}}(x_0) - \xi_{\mathrm{s}}(x_0)\Delta\xi_{\mathrm{c}}(x_0)}{\xi_{\mathrm{c}}^2(x_0) + \xi_{\mathrm{s}}^2(x_0) + \xi_{\mathrm{c}}(x_0)\Delta\xi_{\mathrm{c}}(x_0) + \xi_{\mathrm{s}}(x_0)\Delta\xi_{\mathrm{s}}(x_0)}. \tag{7}$$

Lemma A.2 *It holds that*
$$(\mathbf{A}^\top \mathbf{A})^{-1} = \frac{1}{2p_2 p_3}\begin{pmatrix} (2N - p_2)p_2 & p_1 p_2 \varphi_{\mathrm{c}}(x_0) & p_1 p_2 \varphi_{\mathrm{s}}(x_0) \\ p_1 p_2 \varphi_{\mathrm{c}}(x_0) & p_5 + p_4 \varphi_{\mathrm{c}}(2x_0) & p_4 \varphi_{\mathrm{s}}(2x_0) \\ p_1 p_2 \varphi_{\mathrm{s}}(x_0) & p_4 \varphi_{\mathrm{s}}(2x_0) & p_5 - p_4 \varphi_{\mathrm{c}}(2x_0) \end{pmatrix},$$

where

$$N := n + \frac{1}{2}, \quad p_1 := 1 + 2\sum_{i=1}^{n}\varphi_{\mathrm{c}}(i\Delta x), \quad p_2 := n - \sum_{i=1}^{n}\varphi_{\mathrm{c}}(2i\Delta x),$$

$$p_3 := p_5 - N p_2, \quad p_4 := -p_5 + 2N p_2, \quad p_5 := 2N^2 - \frac{1}{2}p_1^2.$$

Lemma A.3 *It holds that*
$$\Delta g(x_i) = \left(-2\xi_{\mathrm{c}}(x_0)\sin^2\frac{\Delta\phi(x_i)}{2} - \xi_{\mathrm{s}}(x_0)\sin\Delta\phi(x_i)\right)\varphi_{\mathrm{c}}(x_i)$$
$$+ \left(-2\xi_{\mathrm{s}}(x_0)\sin^2\frac{\Delta\phi(x_i)}{2} + \xi_{\mathrm{c}}(x_0)\sin\Delta\phi(x_i)\right)\varphi_{\mathrm{s}}(x_i).$$

Lemma A.4 *It holds that*
$$\mathbf{A}^\top\begin{pmatrix}\Delta g(x_{-n}) \\ \vdots \\ \Delta g(x_n)\end{pmatrix} = -\begin{pmatrix} 0 \\ q_3\xi_{\mathrm{s}}(x_0) + q_4\xi_{\mathrm{c}}(x_0) \\ q_4\xi_{\mathrm{s}}(x_0) + q_3\xi_{\mathrm{c}}(x_0)\end{pmatrix} + \begin{pmatrix} (-q_1\xi_{\mathrm{s}}(x_0) + q_2\xi_{\mathrm{c}}(x_0))\,\varphi_{\mathrm{c}}(x_0) \\ (-q_5\xi_{\mathrm{s}}(x_0) + q_6\xi_{\mathrm{c}}(x_0))\,\varphi_{\mathrm{c}}(2x_0) \\ (-q_6\xi_{\mathrm{s}}(x_0) - q_5\xi_{\mathrm{c}}(x_0))\,\varphi_{\mathrm{c}}(2x_0)\end{pmatrix}$$
$$+ \begin{pmatrix} (q_2\xi_{\mathrm{s}}(x_0) + q_1\xi_{\mathrm{c}}(x_0))\,\varphi_{\mathrm{s}}(x_0) \\ (q_6\xi_{\mathrm{s}}(x_0) + q_5\xi_{\mathrm{c}}(x_0))\,\varphi_{\mathrm{s}}(2x_0) \\ (-q_5\xi_{\mathrm{s}}(x_0) + q_6\xi_{\mathrm{c}}(x_0))\,\varphi_{\mathrm{s}}(2x_0)\end{pmatrix},$$

where

$$q_1 = \sum_{i=-n}^{n}\varphi_{\mathrm{c}}(i\Delta x)\sin\Delta\phi(x_i) + 2\sum_{i=-n}^{n}\varphi_{\mathrm{s}}(i\Delta x)\sin^2\frac{\Delta\phi(x_i)}{2},$$

$$q_2 = \sum_{i=-n}^{n}\varphi_{\mathrm{s}}(i\Delta x)\sin\Delta\phi(x_i) - 2\sum_{i=-n}^{n}\varphi_{\mathrm{c}}(i\Delta x)\sin^2\frac{\Delta\phi(x_i)}{2},$$

$$q_3 = \frac{1}{2}\sum_{i=-n}^{n}\sin\Delta\phi(x_i), \qquad q_4 = \sum_{i=-n}^{n}\sin^2\frac{\Delta\phi(x_i)}{2},$$

$$q_5 = \frac{1}{2}\sum_{i=-n}^{n}\varphi_{\mathrm{c}}(2i\Delta x)\sin\Delta\phi(x_i) + \sum_{i=-n}^{n}\varphi_{\mathrm{s}}(2i\Delta x)\sin^2\frac{\Delta\phi(x_i)}{2},$$

$$q_6 = \frac{1}{2}\sum_{i=-n}^{n}\varphi_{\mathrm{s}}(2i\Delta x)\sin\Delta\phi(x_i) - \sum_{i=-n}^{n}\varphi_{\mathrm{c}}(2i\Delta x)\sin^2\frac{\Delta\phi(x_i)}{2}.$$

Lemma A.5 *When Δx tends to be zero,*

$$
\begin{aligned}
\Delta \xi_{\mathrm{c}}(x_0) &= b(x_0)\{R\cos(\phi(x_0) + 4\pi f x_0) - S\sin(\phi(x_0) + 4\pi f x_0)\} \\
&\quad + R\xi_{\mathrm{c}}(x_0) - S\xi_{\mathrm{s}}(x_0) + \mathcal{O}(\Delta x^5), \\
\Delta \xi_{\mathrm{s}}(x_0) &= b(x_0)\{-S\cos(\phi(x_0) + 4\pi f x_0) - R\sin(\phi(x_0) + 4\pi f x_0)\} \\
&\quad + S\xi_{\mathrm{c}}(x_0) + R\xi_{\mathrm{s}}(x_0) + \mathcal{O}(\Delta x^5),
\end{aligned}
$$

where

$$
R = \frac{p_1 q_2}{4 p_3} + \frac{N\Delta x^2}{p_2 p_3}\sum_{i=1}^{n} i^2 (q_6 - q_4) + \frac{2N\Delta x^4}{3 p_2 p_3}\sum_{i=1}^{n} i^4 \sum_{i=-n}^{n}\sin^2\frac{\Delta\phi(x_i)}{2},
$$

$$
S = \frac{p_1 q_1}{4 p_3} + \frac{N\Delta x^2}{p_2 p_3}\sum_{i=1}^{n} i^2 (q_5 + q_3) - \frac{N\Delta x^4}{3 p_2 p_3}\sum_{i=1}^{n} i^4 \sum_{i=-n}^{n}\sin\Delta\phi(x_i).
$$

Thus, if terms with $\mathcal{O}(\Delta x^5)$ are ignored, we have Eq.(4). ∎

B Supplement to Geometric Interpretation

If terms with $\mathcal{O}(\Delta x^5)$ are ignored, Lemma A.5 yields

$$
\begin{aligned}
\begin{pmatrix} \Delta\xi_{\mathrm{c}}(x_0) \\ \Delta\xi_{\mathrm{s}}(x_0) \end{pmatrix} &= b(x_0)\begin{pmatrix} R & -S \\ -S & -R \end{pmatrix}\begin{pmatrix} \cos(2\theta - \phi(x_0)) \\ \sin(2\theta - \phi(x_0)) \end{pmatrix} + \begin{pmatrix} R & -S \\ S & R \end{pmatrix}\begin{pmatrix} \xi_{\mathrm{c}}(x_0) \\ \xi_{\mathrm{s}}(x_0) \end{pmatrix} \\
&= b(x_0)\begin{pmatrix} R & -S \\ -S & -R \end{pmatrix}\begin{pmatrix} \cos 2\theta \cos\phi(x_0) + \sin 2\theta \sin\phi(x_0) \\ \sin 2\theta \cos\phi(x_0) - \cos 2\theta \sin\phi(x_0) \end{pmatrix} + \begin{pmatrix} R & -S \\ S & R \end{pmatrix}\begin{pmatrix} \xi_{\mathrm{c}}(x_0) \\ \xi_{\mathrm{s}}(x_0) \end{pmatrix} \\
&= \begin{pmatrix} R & S \\ -S & R \end{pmatrix}\begin{pmatrix} \cos 2\theta & \sin 2\theta \\ -\sin 2\theta & \cos 2\theta \end{pmatrix}\begin{pmatrix} \xi_{\mathrm{c}}(x_0) \\ \xi_{\mathrm{s}}(x_0) \end{pmatrix} + \begin{pmatrix} R & -S \\ S & R \end{pmatrix}\begin{pmatrix} \xi_{\mathrm{c}}(x_0) \\ \xi_{\mathrm{s}}(x_0) \end{pmatrix}.
\end{aligned}
$$

We can easily confirm that

$$
\frac{1}{\sqrt{R^2 + S^2}}\begin{pmatrix} R & S \\ -S & R \end{pmatrix} \quad \text{and} \quad \frac{1}{\sqrt{R^2 + S^2}}\begin{pmatrix} R & -S \\ S & R \end{pmatrix}
$$

are the rotation matrices of angle $-\beta$ $(= \arctan(S/R))$ and β, respectively. Moreover,

$$
\begin{pmatrix} \cos 2\theta & \sin 2\theta \\ -\sin 2\theta & \cos 2\theta \end{pmatrix}
$$

is the rotation matrix of angle -2θ. Thus Eq.(6) holds.

References

[1] M. Takeda, H. Ina, and S. Kobayashi, "Fourier-Transform Method of Fringe-Pattern Analysis for Computer-Based Topography and Interferometry," Journal of Optical Society of America **72**(1), 156–160 (1982).

[2] J. Kato, I. Yamaguchi, T. Nakamura, and S. Kuwashima, "Video-Rate Fringe Analyzer Based on Phase-Shifting Electronic Moiré Patterns," Applied Optics **36**(32), 8403–8412 (1997).

[3] D. C. Williams, N. S. Nassar, J. E. Banyard, and M. S. Virdee, "Digital Phase-Step Interferometry: A Simplified Approach," Optics & Laser Technology **23**(3), 147–150 (1991).

[4] N. Brock, J. Hayes, B. Kimbrough, J. Millerd, M. North-Morris, M. Novak, and J. C. Wyant, "Dynamic Interferometry," in *Novel Optical Systems Design and Optimization VIII, Proceedings of SPIE*, J. M. Sasián, R. J. Koshel, and R. C. Juergens, eds., vol. 5875, pp. 1–10 (2005).

[5] M. Sugiyama, H. Ogawa, K. Kitagawa, and K. Suzuki, "Single-shot Surface Profiling by Local Model Fitting," Applied Optics **45**(31), 7999–8005 (2006).

[6] J. H. Brunning, D. R. Herriott, J. E. Gallagher, D. P. Rosenfeld, A. D. White, and D. J. Brangaccio, "Digital Wave Front Measuring Interferometer for Testing Optical Surface and Lenses," Applied Optics **13**(11), 2693–2703 (1974).

[7] K. Goldberg and J. Bokor, "Fourier-transform Method of Phase-shift Determination," Applied Optics **40**(17), 2886–2894 (2001).

[8] A. Albert, *Regression and the Moore-Penrose Pseudoinverse* (Academic Press, New York and London, 1972).

[9] M. Takeda and T. Abe, "Phase Unwrapping by a Maximum Cross-Amplitude Spanning Tree Algorithm: A Comparative Study," Optical Engineering **35**(8), 2345–2351 (1996).

[10] J. O. Smith, *Introduction to Digital Filters* (W3K Publishing, 2007).

[11] G. Wahba, *Spline Model for Observational Data* (Society for Industrial and Applied Mathematics, Philadelphia and Pennsylvania, 1990).

[12] M. Servin, J. L. Marroquin, and F. J. Cuevas, "Demodulation of a Single Interferogram by Use of a Two-dimensional Regularized Phase-tracking Technique," Applied Optics **36**(19), 4540–4548 (1997).